




# Mechanochemical synthesis, characterization, and thermal behavior of meloxicam cocrystals with salicylic acid, fumaric acid, and malic acid

Richard Perosa Fernandes<sup>1</sup> · André Luiz Carneiro Soares do Nascimento<sup>1</sup> · Ana Carina Sobral Carvalho<sup>1</sup> · José Augusto Teixeira<sup>1</sup> · Massao Ionashiro<sup>1</sup> · Flávio Junior Caires<sup>1,2</sup> 

Received: 9 September 2018 / Accepted: 15 February 2019 / Published online: 2 March 2019  
© Akadémiai Kiadó, Budapest, Hungary 2019

## Abstract

A liquid-assisted grinding approach was used to synthesize three cocrystals between the coformers: salicylic acid, fumaric acid, and malic acid with meloxicam, a nonsteroidal anti-inflammatory drug. The spectroscopic techniques, Raman and Fourier transform infrared (FTIR), confirm the formation of these compounds by showing evidence of hydrogen bonds between NH or OH and CO groups. Powder X-ray diffraction verified the formation of the cocrystals by comparing the results with a crystallographic database. Differential scanning calorimetry (DSC), simultaneous thermogravimetry and differential scanning calorimetry (TG-DSC), evolved gas analysis (EGA by TG-FTIR), DSC-photovisual analysis, and videos of the cocrystals being heated were used to study the thermal behavior, analyze the composition, identify polymorphic transitions in meloxicam cocrystal with malic acid, and understand the decomposition phenomena of these solids. The malic acid compound shows a unique degradation step that was confirmed by TG-DSC data and FTIR analysis of the residue formed. A solubility test was performed: fumaric cocrystal showed an enhanced performance compared to pure drug, and malic and salicylic cocrystals showed a slower dissolution profile.

**Keywords** Cocrystal · Fumaric acid · Malic acid · Meloxicam · Salicylic acid · Thermal analysis

## Introduction

Research related to cocrystals has significantly increased over the past years. This is partly due to the growing interest of the pharmaceutical industry in the possibility of modifying the physical properties of pharmaceutical assets through the use of this methodology [1–3]. Cocrystals are crystalline materials composed of two or more different molecules. Typically, they have an active pharmaceutical ingredient (API) and cocrystal formers (“coformers”) in the same crystal lattice [4]. The most important factor

reported for this approach is the possibility of improving properties such as chemical stability, solubility, dissolution rate, and bioavailability, without modifying the therapeutic properties of the API. This may be possible, because these solids are formed through noncovalent interactions [5, 6].

Almost 70% of the APIs are classified as Biopharmaceutical Classification System II (BCS II) [7], with aqueous solubility lower than  $0.1 \text{ mg mL}^{-1}$ , which limits the clinical performance of these compounds. Given this context, the strategy of using pharmaceutical cocrystals to improve the solubility and dissolution rate has been widely used in BCS II drugs [8]. In addition, there are reports of cocrystals with modified melting points, hygroscopicity, and compression behaviors [9–11].

In this context, meloxicam, a nonsteroidal anti-inflammatory drug (NSAID), was originally developed by Boehringer Ingelheim, and it is prescribed to treat rheumatoid arthritis, osteoarthritis, postoperative pains, and fever. The pharmacologically pure substance exists as a yellow solid which is substantially insoluble in water. It is classified as a BCS II, and its solubility is highly dependent on pH because it has multiple ionization states [11–13].

**Electronic supplementary material** The online version of this article (<https://doi.org/10.1007/s10973-019-08118-7>) contains supplementary material, which is available to authorized users.

✉ Flávio Junior Caires  
flavio.caires@unesp.br

<sup>1</sup> Universidade Estadual Paulista (Unesp), Instituto de Química, CP 355, Araraquara, SP 14801-970, Brazil

<sup>2</sup> Universidade Estadual Paulista (Unesp), Faculdade de Ciências, Bauru, SP 17033-260, Brazil

Several reports have attempted to alter the pharmacokinetic profile of meloxicam by complexation, solvation, and synthesis or production of salts [11, 14–17]. The preparation of polymorphic crystal forms is described. However, improvement in the dissolution profile of these compounds has not been promising. Thus, some approaches with cocrystals have been used and have demonstrated an improved dissolution rate that could improve oral absorption of the API. There are literature reports where grinding or solvent-assisted milling is used to produce meloxicam cocrystals with various coformers such as succinic, maleic, benzoic, glycolic, fumaric, hydrocinamic, and other acids [9–11].

In the present article, we report the synthesis, characterization, and thermo-analytical study of three meloxicam (MLX) cocrystals using the coformers: salicylic acid (SLY), fumaric acid (FUM), and malic acid (MLC) as shown in Fig. 1.

The characterization was performed by powder X-ray diffraction (PXRD), Fourier transform infrared spectroscopy (FTIR), Raman spectroscopy, and thermo-analytical techniques that include simultaneous thermogravimetry and differential scanning calorimetry (TG-DSC), differential scanning calorimetry (DSC), and DSC-photovisual analysis. Some coformers previously cited are already reported in the literature. However, different characterization results are presented in this article, and no previous work has reported a systematic thermo-analytical study of these cocrystals. It is important to mention that only few reports discuss the thermal behavior of cocrystals, even though these studies have been reported to be important research that was done in order to

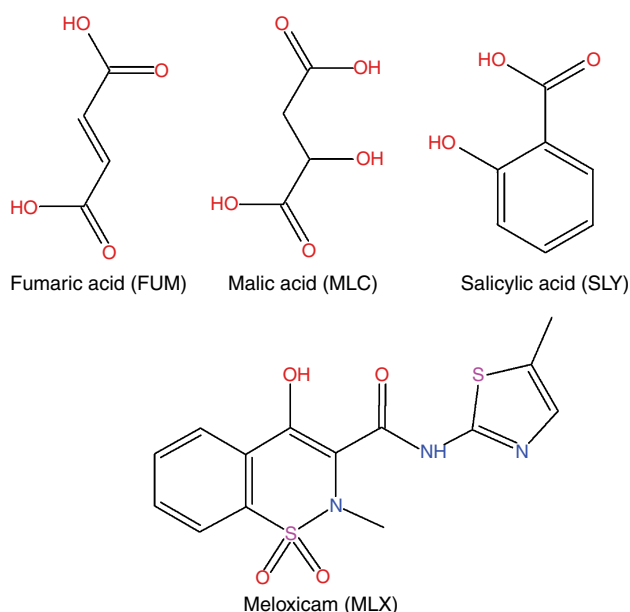


Fig. 1 Chemical structures of compounds

comprehend physical and chemical stability, improve knowledge of drying steps, avoid possible problems with long-term stability, and provide information to understand and develop enhanced solid-state systems [18–20].

## Experimental

### Synthesis

The cocrystals were synthesized by liquid-assisted grinding (LAG). Meloxicam was reacted with three selected coformers: SLY, FUM, and MLC. All reagents and solvents were 98% pure and were obtained from Sigma-Aldrich (São Paulo, Brazil). The mixtures were prepared with a 1:1 stoichiometric ratio (MLX/coformer) with 450 mg of total mass and 112  $\mu\text{L}$  of solvent. Tetrahydrofuran was the solvent for MLX/FUM, and ethanol was used for MLX/SLY and MLX/MLC. The LAG methodology was followed with  $\eta = 0.25$  v:m (total solvent/total mass) [21]. The reagents were ground at a frequency of 15 Hz for 30 min using a Retsch MM 200 mill with 10 mL stainless steel jars and one 7 mm stainless steel sphere. The cocrystals were then dried at 50  $^{\circ}\text{C}$  for 8 h to remove any residual solvent.

### Experimental equipment and conditions

Thermogravimetric and differential scanning calorimetry analyses were obtained with two thermal analysis systems: simultaneous thermogravimetry and differential scanning calorimetry TG-DSC 1 (Mettler Toledo) and DSC Q10 (TA Instruments). Two types of purge gases were used: dynamic dry air and nitrogen for TG-DSC and only nitrogen for DSC. Both were used at a flow rate of 50  $\text{mL min}^{-1}$ . A heating rate of 10  $^{\circ}\text{C min}^{-1}$  was adopted. Samples weighed about 10 mg for TG-DSC and 2 mg for DSC. Alumina and aluminum crucibles, the latter with a perforated cover, were used to record the TG-DSC and DSC curves, respectively.

The DSC-photovisual analysis was obtained using a Mettler Toledo DSC 1 stare system coupled to an OLYMPUS digital camera, model SC 30, which incorporates a 3.3-megapixel CMOS sensor and an optical sub-assembly mechanic Navitar 1-6232D with 6.5  $\times$  zoom. The experimental conditions were similar to those used to obtain the DSC curve.

The videos were made with a device adapted in our laboratory. It consisted of digital melting-point equipment from Micro Quimica which was used to heat the sample and a digital camera from Asus, model ze55ek1, that was used to record the videos. The experimental conditions used to obtain the videos were as follows: heating rate of

0.5 °C min<sup>-1</sup>, a static air atmosphere, a small beaker for the sample holder, resolution of 480 pixels, 30 frames per second, and clip speed 7.0 × runtime.

The evolved gas analysis (EGA by TG-FTIR) of products released during the thermal decomposition of the cocrystals was carried out using a TG-DSC 1 Mettler Toledo coupled to a Nicolet FTIR spectrophotometer with a gas cell and a DTGS KBr detector. The furnace and heated gas cell (250 °C) were coupled through a heated (225 °C) 120 cm stainless steel transfer line with a diameter of 3.0 mm that was purged with dynamic dry air (50 mL min<sup>-1</sup>). The FTIR spectra were recorded with 16 scans per spectrum at a resolution of 4 cm<sup>-1</sup>. Identification of the gaseous products was based on the reference spectra available in the spectrometer software (OMNIC 8.0) and literature data.

Powder X-ray diffractograms were obtained using a Rigaku MiniFlex II X-ray diffractometer (Rigaku Corporation) employing CuK $\alpha$  radiation ( $\lambda = 1.54056 \text{ \AA}$ ) with a setting of 40 kV and 30 mA. The samples were analyzed from 5° to 50° (2 $\theta$ ) with a scanning speed of 2° min<sup>-1</sup> (continuous scan mode).

Infrared spectra were obtained using a Nicolet iS10 FTIR spectrophotometer using an ATR accessory with a Ge window. The FTIR spectra were recorded with 32 scans per spectrum at a resolution of 4 cm<sup>-1</sup>.

The Raman spectroscopy analyses were performed in a RAMMI spectrophotometer (Bruker, Germany). The system was equipped with a helium–neon laser operating at the 1064 nm line for excitation and a Ge detector cooled with liquid nitrogen. The slits were set for a 2 cm<sup>-1</sup> spectral resolution with 200 mW power and 512 scans. The spectra were recorded using the spectral range between 200 and 3400 cm<sup>-1</sup>. The powder samples (pure components and cocrystals) were placed in a glass tube for analysis in a scattering geometry and collected at 90°.

Solubility study experiments were conducted in 50 mM sodium phosphate buffer solution at pH 6.7 and 37 °C to simulate intestinal physiological conditions [22]. In each dissolution experiment, an excess of the crystalline solid and 12 mL of buffer solution were used. The amount of solid introduced in each falcon tube was sufficient to maintain a supersaturated solution for the duration of the study. Three replicates of each material were prepared. The study was performed in a KASVI Thermo Shaker (São José dos Pinhais, Brazil), model K80-200, set to 500 rpm. Approximately 1 mL of sample solution was taken at 6, 12, 18, and 24 h. The samples were filtered through a 0.45- $\mu$ m nylon filter and diluted for further quantification. After each sampling, the volume of the liquid removed was compensated with buffer solution. Solution samples were analyzed with a spectrophotometer LAMBDA 1050

(Waltham, USA), and the maximum absorbance was measured at 366 nm.

## Results and discussion

### Meloxicam (MLX)

The TG-DSC curves of the pure meloxicam drug obtained in dynamic dry air and in a N<sub>2</sub> atmosphere are shown in Fig. 2. These curves indicate that the drug is thermally stable up to 230 °C in both atmospheres. Above this temperature, the thermal decomposition occurs in two consecutive and overlapped steps between 230–360 °C ( $\Delta m_1 = 75.31\%$ ) and 360–600 °C ( $\Delta m_2 = 22.58\%$ ) in air atmosphere and 230–360 °C ( $\Delta m_1 = 74.08\%$ ) and 360–800 °C ( $\Delta m_2 = 9.23\%$ ) in N<sub>2</sub> atmosphere. The first step was attributed to the thermal decomposition of the drug and was associated with the exothermic peak at 267 °C in the DSC curve.

The second step of mass loss in the TG curve is strongly influenced by the atmosphere used. In air atmosphere, it is attributed to oxidation of the carbonized material formed in the previous step, corresponding to the exothermic peak in the DSC curve, while in an inert atmosphere, it is attributed to a slow pyrolysis process without any corresponding thermal event on the DSC curve.

A DSC curve (Fig. 3) with an endothermic peak at 261 °C shows an enthalpy of 35.0 kJ mol<sup>-1</sup> that is attributed to the incongruent fusion of meloxicam and this is in agreement with a previous report [23].

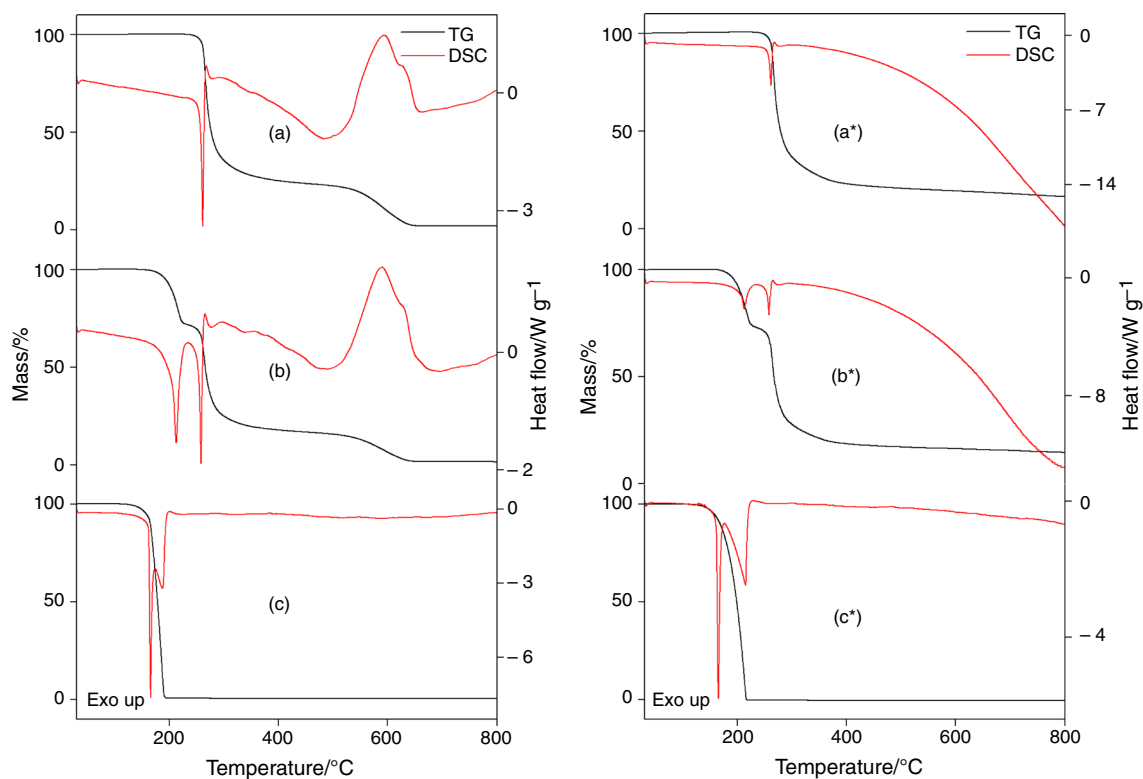
PXRD analysis (Fig. S1) shows that the drug meloxicam used in this work is in the polymorphic form I, the form marketed in pharmaceuticals [11], with maximum intensity at 2 $\theta$  equal to 15° and 25.8°. The peak at 13° present in meloxicam form III was not found, which confirms that the precursor is in form I.

The FTIR and Raman spectra of meloxicam are shown in Fig. 4, and the assignments of the main bands are listed in Table S1. Characteristic vibrational modes of the pure compound, such as  $\nu$  O–H<sub>enol</sub> at 3290 cm<sup>-1</sup>,  $\nu$  C=O +  $\delta$  N–H at 1621 cm<sup>-1</sup>,  $\nu$  C–H<sub>thiazole ring</sub> at 2999 cm<sup>-1</sup>,  $\nu$  C–H<sub>(CH<sub>3</sub> group)</sub> at 2968 cm<sup>-1</sup>, and  $\nu$  SO<sub>2</sub> at 1344 cm<sup>-1</sup> were identified, and all were in agreement with previously reported data [12, 23].

### SLY and MLX/SLY (1:1)

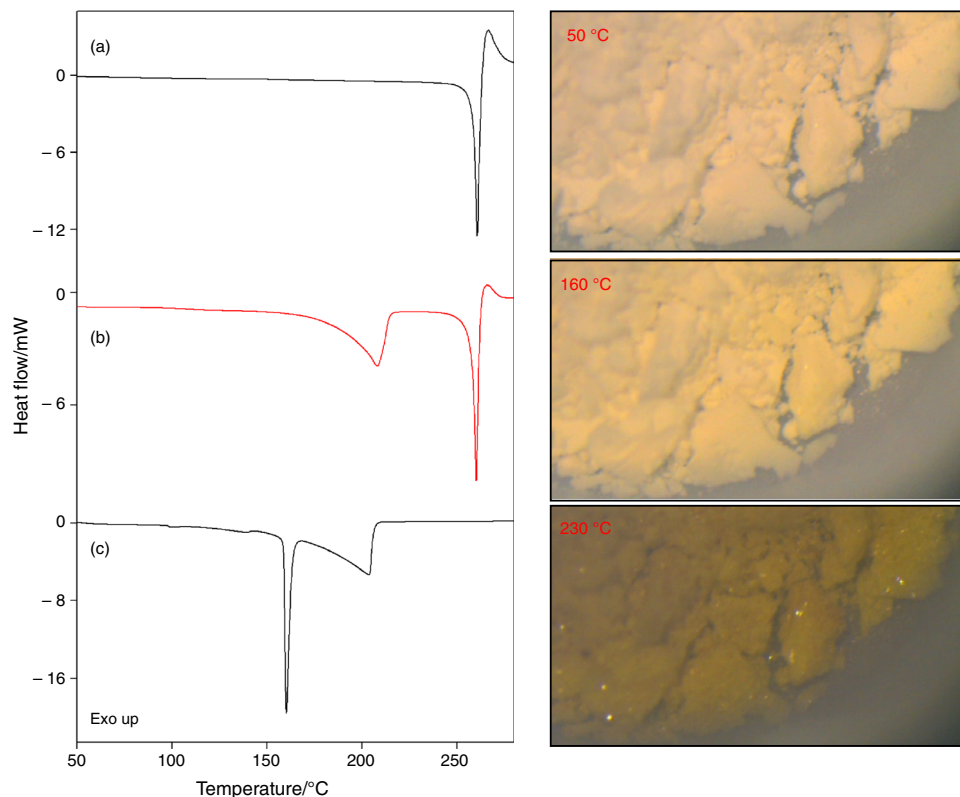
The TG-DSC curves of the SLY, MLX, and MLX/SLY (1:1) systems obtained in dynamic dry air and nitrogen atmosphere are shown in Fig. 2.

The TG-DSC curves of the salicylic acid in both atmospheres show that the compound is thermally stable up



**Fig. 2** TG-DSC curves obtained in air and in N<sub>2</sub>\* atmospheres: (a, a\*) MLX (10.0097, 9.9695\* mg), (b, b\*) MLX/SLY (1:1) cocrystal (10.0023, 10.0039\* mg), and (c, c\*) SLY (10.0855, 10.0620\* mg)

**Fig. 3** DSC curve of **a** MLX, **b** MLX/SLY (1:1) cocrystal, **c** SLY and images obtained by DSC-photovisual analysis of MLX/SLY(1:1) cocrystal



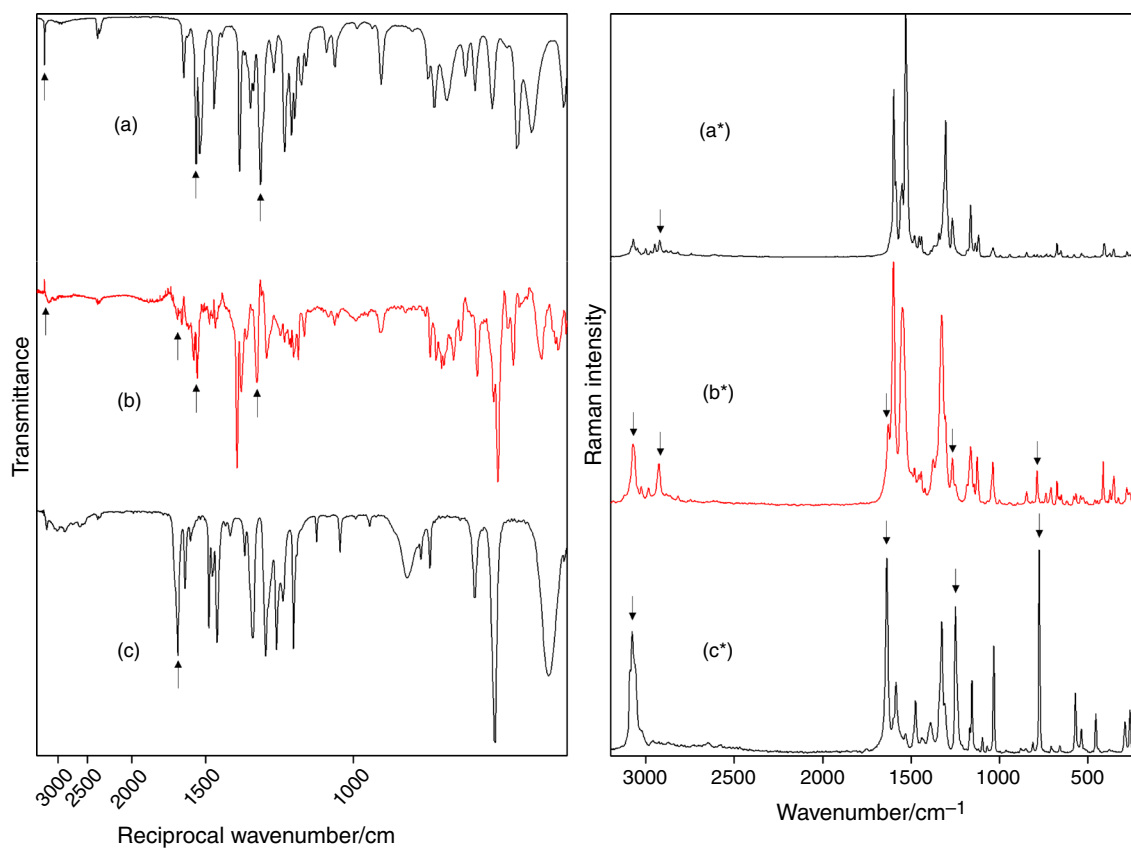


**Fig. 4** FTIR and Raman\* spectra for (a, a\*) MLX, (b, b\*) MLX/SLY (1:1) cocrystal, and (c, c\*) SLY

to 110 °C. Above this temperature, the total mass loss occurs in a single step, corresponding to an endothermic peak at 186 °C in the DSC curve. This was attributed to partial sublimation and evaporation of the compound. The endothermic peak at 166 °C in the DSC curve corresponds to the melting of the compound.

The TG-DSC curves of the MLX/SLY (1:1) system that were obtained in a dynamic dry air atmosphere have a different thermal behavior from the pure components. These changes suggest the formation of a cocrystal, because a multicomponent system exhibits a different profile than the individual components and is not just the sum of them [24]. The TG curves show that the thermal stability of the MLX/SLY (1:1) system is higher than coformer and lower than MLX up to 150 °C. Above this temperature, the thermal decomposition occurs in three consecutive and overlapping steps between 150 and 670 °C. The steps correspond to endothermic and exothermic events in the DSC curve. The first mass loss between 150 and 236 °C corresponds with an endothermic peak at 214 °C. It is attributed to the thermal decomposition of the MLX/SLY system with release of SLY ( $\Delta m_{\text{TG}} = 28.09\%$ ,  $\Delta m_{\text{Theor.}} = 28.21\%$ ). The mass loss confirms the 1:1 stoichiometry of the cocrystal. The second (236–420 °C) and third (420–670 °C) steps of mass loss

correspond to endothermic (258 °C) and exothermic peaks (265 and 590 °C) in the DSC curve. These are attributed to thermal decomposition and oxidation of the API ( $\Delta m_{\text{TG}} = 71.91\%$ ,  $\Delta m_{\text{Theor.}} = 71.79\%$ ), and the steps are very similar to those observed in the TG-DSC curves of the pure drug.

The TG-DSC curve obtained in nitrogen atmosphere shows that the thermal behavior of the MLX/SLY(1:1) system is very similar to that presented in the dynamic dry air atmosphere, at least up to the first two stages. The third mass loss, without a thermal event in the DSC curve, is attributed to the slow pyrolysis of the carbonized material formed in the previous step due to thermal decomposition of the drug.

In addition, to discard the formation of solvate cocrystal or the presence of residual solvent in the material, an EGA of MLX/SLY was performed (Fig. S2). The only gaseous products identified were carbon dioxide, carbon monoxide, and carbonyl sulfide. Characteristic absorption bands of ethanol molecules were not observed. This rejects the presence of solvent in the synthesized cocrystal.

The DSC curves of the SLY, MLX, and MLX/SLY (1:1) systems are shown in Fig. 3. The DSC curve of SLY shows two endothermic peaks at 160 °C ( $\Delta H = 19.29 \text{ kJ mol}^{-1}$ ) and 219 °C ( $\Delta H = 34.37 \text{ kJ mol}^{-1}$ ) that are attributed to



melting and evaporation of the remaining material, respectively.

The DSC curve of the MLX/SLY (1:1) system shows two endothermic peaks. The first one at 207 °C ( $\Delta H = 63.64 \text{ kJ mol}^{-1}$ ) is attributed to cocrystal decomposition with a release of SLY from the system. The second at 259 °C ( $\Delta H = 44.78 \text{ kJ mol}^{-1}$ ) is attributed to the incongruent melting of the meloxicam drug. In addition, thermal events associated with the melting of the coformer were not observed on DSC curve, which suggests the formation of the cocrystal. All peak temperatures and enthalpy values are further described in Table S2.

The images obtained by DSC-photovisual analysis (Fig. 3) and the video of the MLX/SLY (1:1) system being heated (Supplementary Material) show that after the first endothermic event at 230 °C, the sample has a brighter appearance which is a result of the thermal decomposition of the cocrystal. As can be seen in the video, part of the material evaporates and condenses on the vessel wall and solidifies into a needle shape during cooling. The crystals were collected and analyzed by FTIR. The infrared spectrum of the collected material is identical to the spectrum of SLY, confirming the decomposition of the MLX/SLY (1:1) system with release of salicylic acid.

The powder X-ray diffractograms of the pure components and of the MLX/SLY (1:1) system are presented in the Supplementary Material (Fig. S3). The diffractogram of the MLX/SLY (1:1) system presents new peaks at 8.6°, 9.3°, 11.8°, 12.7°, 14.4°, 16.3°, 23.3°, 26.7°, 28.8°, 33.6°, 34.5°, 35.8°, and others that differ from the pure components but are not just the sum of the diffractograms of the isolated components. This confirms the formation of the MLX/SLY (1:1) cocrystal through LAG methodology [25]. In addition, when comparing the diffractogram of MLX/SLY (1:1) with the previously reported cocrystal (Fig. S4) [9], the MLX/SLY (1:1) system has similar peaks and this confirms that form III of the MLX/SLY (1:1) cocrystal was obtained.

The FTIR spectra for the cocrystal and the pure components are shown in Fig. 4. The C=O stretching band at  $1653 \text{ cm}^{-1}$  (SLY) and N–H stretching band at  $3290 \text{ cm}^{-1}$  (MLX) are not observed in the cocrystal spectrum; this may indicate the establishment of hydrogen bonding between the groups N–H (MLX) and C=O (SLY) in the cocrystal structure, since this type of interaction has already been reported in cocrystal formation [3]. The bands at  $1550$  and  $1529 \text{ cm}^{-1}$  in MLX appear shifted to higher energies at  $1562$  and  $1539 \text{ cm}^{-1}$  in the MLX/SLY (1:1) spectrum, and the band assigned to  $\nu \text{ SO}_2$  changes from  $1263 \text{ cm}^{-1}$  in MLX to  $1277 \text{ cm}^{-1}$  in the MLX/SLY (1:1) spectrum. Other changes occur between the pure components and the cocrystal, with all the principal vibrations described in Table S2.

The Raman spectra of SLY, MLX/SLY (1:1) cocrystal, and MLX are shown in Fig. 4. The strong band at  $3073 \text{ cm}^{-1}$  from SLY spectrum, attributed to aromatic C–H stretching ( $\nu_{\text{ar}} \text{ C–H}$ ), has its intensity decreased in the cocrystal spectrum, while the bands at around  $2925 \text{ cm}^{-1}$ , attributed to C–H stretching ( $\text{CH}_3$  group), have their intensity increased in the cocrystal spectrum. The significant decrease in the  $\nu \text{ C=O}$  (carboxylic group) at  $1637 \text{ cm}^{-1}$  suggests that this group interacts with meloxicam as already observed in infrared spectra. Changes in the bands attributed to out-of-phase CCO stretching ( $\nu_{\text{oop}} \text{ CCO}$ ) were observed, with an intensity increase in the band in  $1322 \text{ cm}^{-1}$  and  $1308 \text{ cm}^{-1}$ , and the disappearance of the band at  $1246 \text{ cm}^{-1}$ . Interestingly, the same increase in  $\nu_{\text{oop}} \text{ CCO}$  was not seen in the intense band at  $771 \text{ cm}^{-1}$  assigned as CCO stretching, which disappears in the cocrystal. Some bands were not observed in the cocrystal, such as the aromatic C=C ring stretching ( $\nu_{\text{CC ring}}$ ) at  $1584 \text{ cm}^{-1}$ ,  $1024 \text{ cm}^{-1}$  and angular deformation of CCO group ( $\delta \text{ CCO}$ ) at  $566 \text{ cm}^{-1}$  and  $457 \text{ cm}^{-1}$ .

### FUM and MLX/FUM (1:1)

The TG-DSC curves of MLX, FUM, and MLX/FUM (1:1) systems obtained in dynamic dry air and  $\text{N}_2$  atmosphere are shown in Fig. 5.

The TG-DSC curves of the fumaric acid in both atmospheres show that the compound is thermally stable up to 200 °C. Above this temperature, the mass loss occurs in a single step between 200 and 310 °C. This corresponds with the endothermic peak at 278 °C on the DSC curve, which is attributed to fusion and evaporation of the compound [26].

The TG-DSC curves of MLX/FUM (1:1) in dynamic air atmosphere show that the system is thermally stable up to 200 °C. Above this temperature, the mass loss occurs in two overlapped steps between 200 and 650 °C. The first mass loss between 200 and 344 °C is attributed to thermal decomposition of the MLX/FUM (1:1) system with release of FUM and decomposition of MLX, respectively ( $\Delta m_{\text{TG}} = 75.48\%$ ,  $\Delta m_{\text{Theor.}} = 75.31\%$ ); this step confirms the 1:1 stoichiometry with less than 1% error. The endothermic peak at 244 °C on the DSC curve is associated with incongruent fusion of the MLX/FUM (1:1) system. The second mass loss between 344 and 650 °C ( $\Delta m = 23.41\%$ ) is associated with the exothermic peak at 575 °C, and it is attributed to the oxidation of the carbonized material formed in the previous step.

The TG-DSC curves obtained in nitrogen atmosphere show a profile very similar to those obtained in dynamic dry air atmosphere up to 400 °C. Above 400 °C, the profile changes due to the absence of oxygen that causes the oxidation of the organic matter in the region between 500

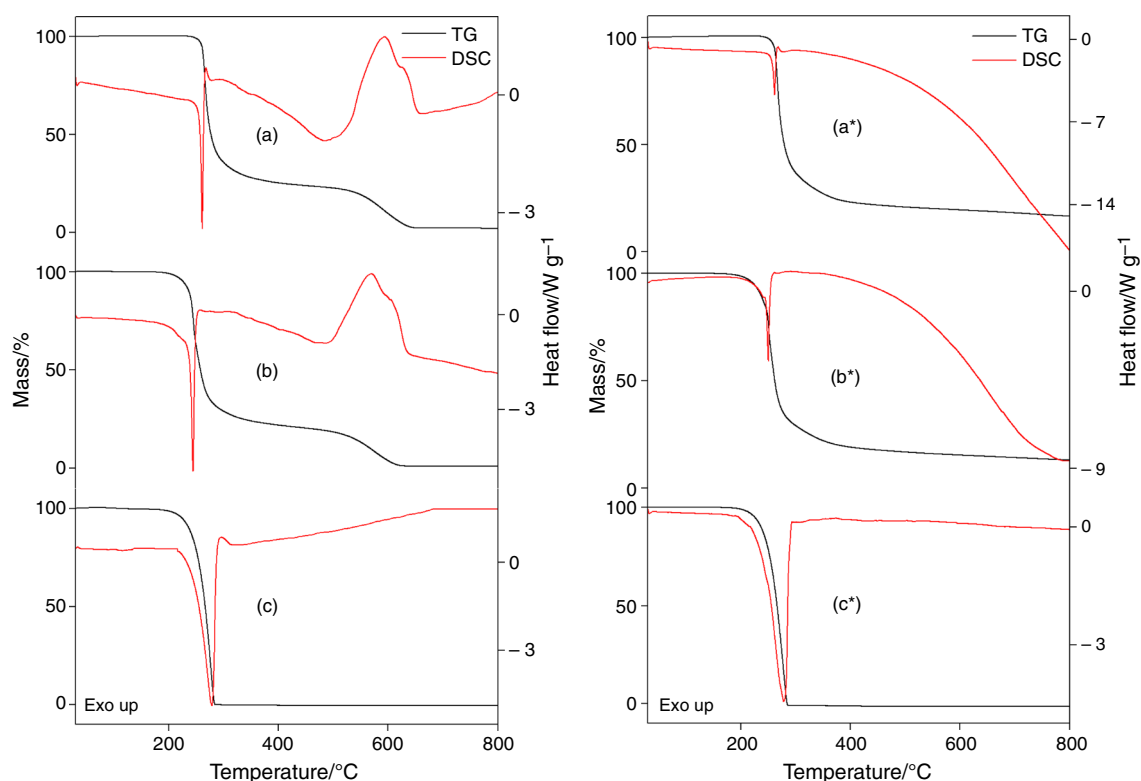


**Fig. 5** TG-DSC curves obtained in air and in N<sub>2</sub>\* atmospheres: (a, a\*) MLX (10.0097, 9.9695\* mg), (b, b\*) MLX/FUM (1:1) cocrystal (10.0023, 10.0039\* mg), and (c, c\*) FUM (10.0855, 10.0620\* mg)

and 700 °C. Mass loss on the TG curve is observed up to 800 °C without any thermal event in the DSC curves. This is attributed to pyrolysis of the carbonized material produced in the previous step.

The EGA of the released gaseous products during the thermal decomposition of MLX/FUM (1:1) in dynamic dry air is shown in Fig. S5. The main products detected were similar to the MLX/SLY (1:1) system with bands at 2400, 1800, and 650 cm<sup>-1</sup> and without signals associated with tetrahydrofuran, which indicates that the solvent is not present in the cocrystal.

The DSC curves of FUM, MLX, and MLX/FUM (1:1) are shown in Fig. 6. The DSC curve of FUM shows an endothermic peak at 280 °C ( $\Delta H = 85.17 \text{ kJ mol}^{-1}$ ) that is attributed to evaporation and melting of the compound, in agreement with the TG-DSC results. On the other hand, the DSC curve of the MLX/FUM (1:1) system contains an endothermic peak at 243 °C ( $\Delta H = 105.93 \text{ kJ mol}^{-1}$ ) that is attributed to the incongruent melting of the MLX/FUM (1:1) system, which occurs at lower temperatures than in the DSC curves of the isolated compounds, as already observed in the TG-DSC curves. Table S2 summarizes all peak temperatures and enthalpy values of the thermal events observed. Also, the video from MLX/FUM system heating is available in the supplementary data.

The powder X-ray diffractograms of the pure components and of the MLX/FUM (1:1) system are presented in the Supplementary Material (Fig. S6). The diffractogram of the MLX/FUM system presents peaks at 11.8°, 13.8°, 14.4°, 16.2°, 26.6°, and others that differ from pure components. The difference in the diffractograms confirmed the formation of the MLX/FUM (1:1) cocrystal.

In addition, a comparison of the diffractogram of the synthesized MLX/FUM (1:1) cocrystal with that of the MLX/FUM (1:1) cocrystal previously reported [9] (Fig. S7) shows a great similarity. However, the peaks at 28° and 29° are only present in the cocrystal diffractogram reported in this article, suggesting the formation of a new polymorphic form.

When compared with pure components, the cocrystal FTIR spectrum (Fig. 7) shows that the C=O stretching at 1662 cm<sup>-1</sup> ( $\nu$  C=O) from FUM and N-H stretching in 3290 cm<sup>-1</sup> ( $\nu$  N-H) from MLX is not observed in the cocrystal spectrum. This may indicate a hydrogen bonding between C=O...H-N in the cocrystal structure. The  $\nu$  C=O +  $\delta$  N-H at 1621 cm<sup>-1</sup> from MLX shows a weaker intensity when compared to cocrystal. Other vibrational frequencies are shown in Table S1.

The Raman spectra of the FUM, MLX, and MLX/FUM (1:1) cocrystal are shown in Fig. 7. The band at 1686 cm<sup>-1</sup> attributed to the  $\nu$  C=O ( $-\text{COOH}$ ) of the FUM is not

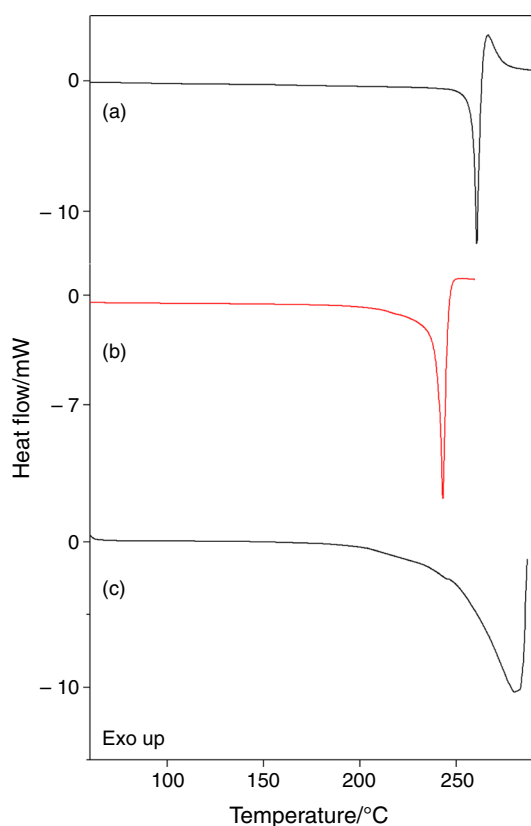


**Fig. 6** DSC curve of **a** MLX, **b** MLX/FUM (1:1) cocrystal, and **c** FUM

observed in the cocrystal spectrum. This suggests that the carboxylic group is involved in the interaction with MLX, which agrees with the FTIR results. The intensity of the band at  $3072\text{ cm}^{-1}$  attributed to C–H stretching ( $\nu$  C–H) decreases, while the bands in the region between  $1000$  and  $300\text{ cm}^{-1}$  are not observed in the cocrystal spectrum. Compared to MLX, there are significant changes in the region between  $1600$  and  $1200\text{ cm}^{-1}$ . The bands at  $1530\text{ cm}^{-1}$  ( $\nu_{\text{thiazole}} + \delta$  N–H +  $\delta$  C–H<sub>CH<sub>3</sub>group</sub>),  $1344\text{ cm}^{-1}$  ( $\nu$  SO<sub>2</sub>), and  $1550\text{ cm}^{-1}$  ( $\delta$  O–H +  $\nu$  C–H<sub>ar</sub> +  $\nu$  C=C<sub>ar</sub>) have increased intensity in the cocrystal spectrum.

### MLC and MLX/MLC (1:1)

The TG-DSC curves of the MLX, MLC, and MLX/MLC (1:1) systems that were obtained in dynamic dry air and N<sub>2</sub> atmosphere are shown in Fig. 8.

The TG-DSC curves of the MLC in both atmospheres show that the compound is thermally stable up to  $155\text{ }^{\circ}\text{C}$ . Above this temperature, the total mass loss occurs in a single step that corresponds with the endothermic peaks at  $232\text{ }^{\circ}\text{C}$  and  $253\text{ }^{\circ}\text{C}$  on the DSC curve. This is attributed to evaporation of the material. The endothermic peak at

$140\text{ }^{\circ}\text{C}$ , without mass loss on the TG curve, corresponds to the melting of the compound.

As few papers report the thermal behavior of this compound, a deep thermal study was performed for the MLC cocrystal. The video (available in the Supplementary Material) of malic acid being heated to  $250\text{ }^{\circ}\text{C}$  illustrates that it melts and partially evaporates (condenses on the vessel wall). The evaporated material that condensed on the vessel wall and the residue remaining in the vessel bottom after cooling was analyzed by FTIR (Fig. S8). The FTIR spectrum of the evaporated product has a spectrum similar to maleic acid. The bottom residue showed a spectrum similar to fumaric acid. These results suggest that the fused malic acid decomposes into maleic acid and fumaric acid and that the maleic acid evaporates at a temperature above  $135\text{ }^{\circ}\text{C}$ , but the fumaric acid stays solid up to  $200\text{ }^{\circ}\text{C}$ . This is in agreement with the thermal behavior of both acids, since maleic acid has lower thermal stability than fumaric acid [27]. From these results, a thermal decomposition mechanism of malic acid was proposed and presented in the Supplementary Material (Fig. S9). Furthermore, the formation of these two compounds explains the endothermic peaks observed on the DSC curve of MLC, which corresponds to evaporation and melting of the two products formed.

The TG-DSC curves of the MLX/MLC (1:1) in dynamic dry air atmosphere show that the system is thermally stable up to  $160\text{ }^{\circ}\text{C}$ . Above this temperature, the mass loss occurs in two consecutive and overlapping steps between  $160$  and  $660\text{ }^{\circ}\text{C}$ . The first mass loss between  $160$  and  $300\text{ }^{\circ}\text{C}$  ( $\Delta m_{\text{TG}} = 74.33\%$ ) corresponds with two endothermic peaks at  $212\text{ }^{\circ}\text{C}$  and  $228\text{ }^{\circ}\text{C}$  on DSC curve. It is attributed to the thermal decomposition of the MLX/MLC (1:1) system with a release of MLC and other decomposition products; this mass loss confirms the 1:1 stoichiometry of the cocrystal formed. The endothermic peak at  $137\text{ }^{\circ}\text{C}$ , without mass loss on the TG curve, is attributed to a physical phenomenon, which will be discussed together with DSC-photovisual analysis. The second mass loss between  $300$  and  $660\text{ }^{\circ}\text{C}$  ( $\Delta m_{\text{TG}} = 25.06\%$ ) is associated with the exothermic peak at  $548\text{ }^{\circ}\text{C}$ . It is attributed to the oxidation of carbonized material or of gaseous products evolved.

The TG-DSC curves obtained in nitrogen atmosphere show a profile similar to those obtained in dynamic dry air atmosphere up to around  $300\text{ }^{\circ}\text{C}$ . These curves are associated with the phenomena previously described in air atmosphere. Above  $300\text{ }^{\circ}\text{C}$ , the TG curve indicates a slow mass loss up to  $800\text{ }^{\circ}\text{C}$  ( $\Delta m_{\text{TG}} = 89.62\%$ ) with no thermal event on the DSC curve. This is attributed to the slow pyrolysis of the carbonized material produced in the previous steps.



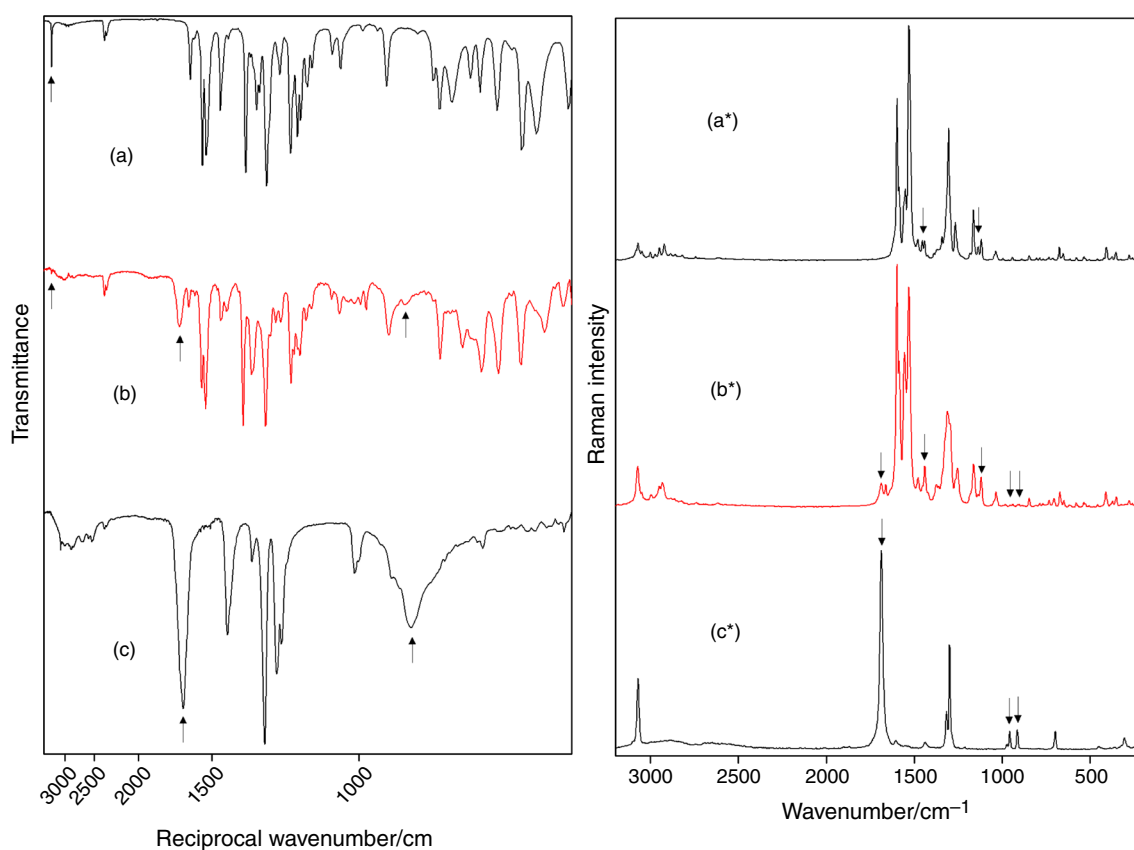


**Fig. 7** FTIR and Raman\* spectra for (a, a\*) MLX, (b, b\*) MLX/FUM (1:1) cocrystal, and (c, c\*) FUM

The EGA of the released gaseous products identified during the thermal decomposition of MLX/MLC (1:1) in dynamic dry air is shown in Supplementary Material (Fig. S10). The main products detected were similar to the MLX/SLY system with bands of CO<sub>2</sub>, CO, and carbonyl sulfide. A high-intensity signal was observed near 1800 cm<sup>-1</sup> that was attributed to some ketone formed in the degradation of the MLX/SLY (1:1) system. Maleic acid was not observed in EGA, probably because it degraded in the heated transfer line.

The DSC curves of MLX, MLC, and MLX/MLC (1:1) are shown in Fig. 9. The DSC curve of malic acid shows two endothermic events. The first peak at 133 °C ( $\Delta H = 30.86 \text{ kJ mol}^{-1}$ ) is attributed to melting of the compound, and the second broad peak at 256 °C ( $\Delta H = 141.73 \text{ kJ mol}^{-1}$ ) is attributed to thermal decomposition, evaporation, and melting, as already discussed in the TG-DSC curves.

The DSC curve of the MLX/MLC (1:1) system is significantly different from the DSC curves of the pure components, which suggests MLX/MLC (1:1) cocrystal formation. The first endothermic peak at 131 °C ( $\Delta H = 17.16 \text{ kJ mol}^{-1}$ ) is attributed to physical phenomenon. The second thermal event with a peak at 211 and 226 °C ( $\Delta H = 120.83 \text{ kJ mol}^{-1}$ ) is attributed to thermal

decomposition of the cocrystal. Table S2 summarizes all peak temperatures and enthalpy values of the thermal events observed.

The results obtained by DSC-photovisual analysis (Fig. 9) and the video of MLX/MLC (1:1) being heated (Supplementary Material) confirm that the first thermal event is not related to the melting of the MLX/MLC (1:1) system or excess coformer, because the sample presents the same physical characteristics up to 150 °C. This thermal event is associated with a polymorphic transition which was confirmed by PXRD analysis of the heated sample at 120 °C (before the thermal event) and 150 °C (after thermal event). The diffractogram (Fig. S11) shows significant changes in the regions near 6.5°, 11.3°, 20.1°, 23°, 25°, 32.7°, and 37.5°. The cyclic DSC experiment indicates that this endothermic event is associated with an irreversible phase transition (Fig. S12) that is probably due to kinetic issues, since up to 120 °C, the polymorph obtained in the synthesis is the most stable phase, and during heating, it absorbs energy (endothermic event) to become stable at higher temperatures. Thus, these two polymorphs have an enantiotropic relationship [28].

The powder X-ray diffractograms of MLC, MLX, and MLX/SLY (1:1) are shown in Fig. S13. The MLX/MLC (1:1) system presents a distinct diffraction pattern when

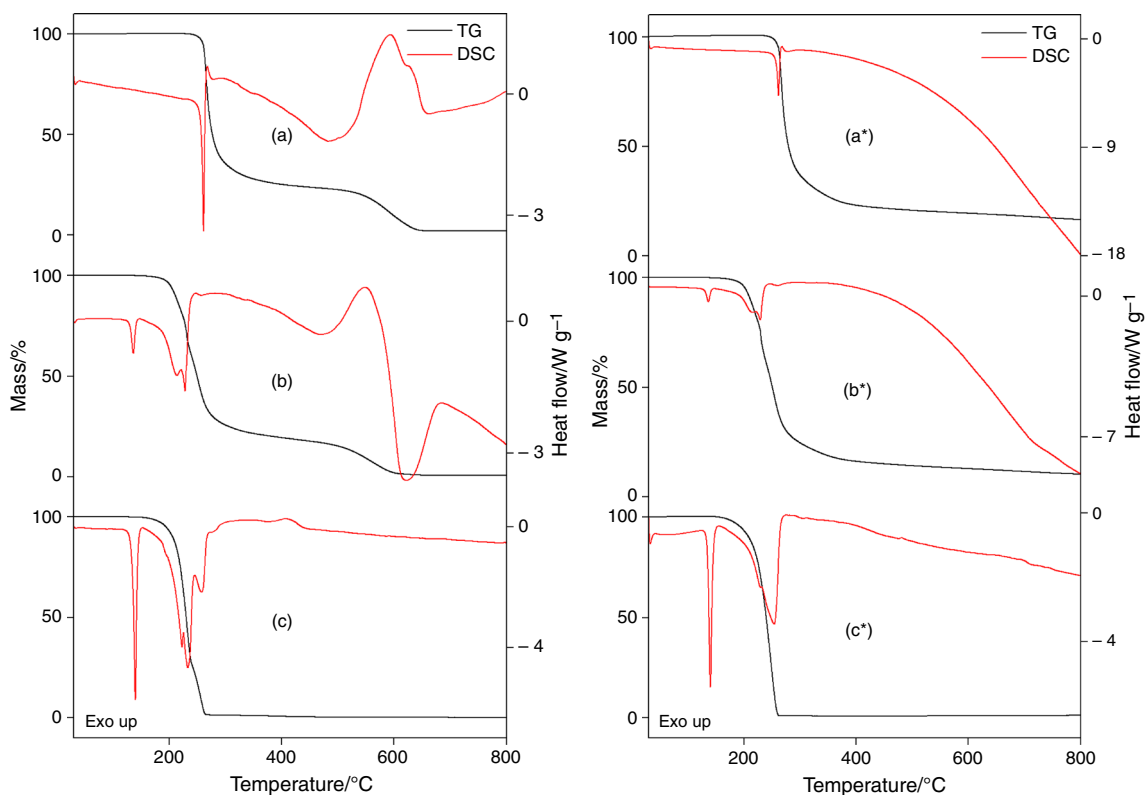
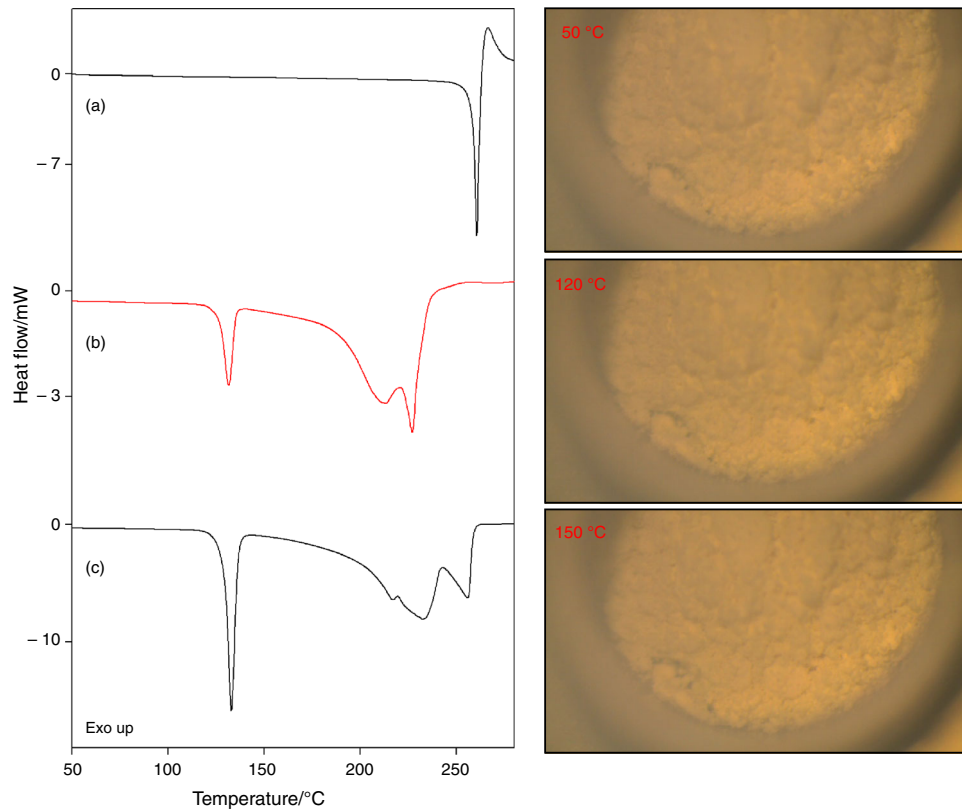


**Fig. 8** TG-DSC curves obtained in air and in  $N_2^*$  atmospheres: (a, a\*) MLX (10.0097, 9.9695\* mg), (b, b\*) MLX/MLC (1:1) cocrystal (10.0082, 9.9805\* mg), and (c, c\*) MLC (9.9695, 10.0820\* mg)

**Fig. 9** DSC curve of **a** MLX, **b** MLX/MLC (1:1) cocrystal, **c** MLC and images obtained by DSC-photovisual analysis of MLX/MLC(1:1) cocrystal



compared to the pure substances. The system has unique peaks at 11.8°, 14.2°, 16.4°, 27.3°, 32.8°, and 33.5°, which confirm cocrystal formation and are in agreement with a previous report [9].

The FTIR and Raman spectra for the cocrystal and the pure components are shown in Fig. 10. The cocrystal FTIR spectrum does not show  $\nu$  O–H from MLX at 3290  $\text{cm}^{-1}$  and  $\nu$  O–H from MLC at 3442 (Fig. 10). The  $\nu$  C=O +  $\delta$  N–H at 1621  $\text{cm}^{-1}$  from MLX shifts to 1635  $\text{cm}^{-1}$ , and the  $\nu$  C=O from MLC shows a weaker signal in MLX/MLC (1:1). These changes suggest a N–H and C=O hydrogen bond between the two compounds in the cocrystal lattice.

The cocrystal Raman spectrum presents a characteristic spectral pattern which indicates the establishment of a new solid-state interaction, as already seen in the FTIR spectrum. The medium- and strong-intensity bands at 2992 ( $\nu_{\text{as}}$  C–H) and 2944  $\text{cm}^{-1}$  ( $\nu_{\text{s}}$  C–H) of CH<sub>2</sub> group from MLC are weaker on the MLX/MLC (1:1) cocrystal spectrum. However, the band at 3073  $\text{cm}^{-1}$  ( $\nu$  C–H) of the CH<sub>3</sub> group from MLX shows a slight increase in intensity. Comparison of MLX and MLX/MLC (1:1) cocrystal spectra finds significant changes in the region between 1600 and 1200  $\text{cm}^{-1}$ , with a weaker band at 1530  $\text{cm}^{-1}$  ( $\nu$  C=C<sub>thiazole ring</sub> +  $\delta$  N–H +  $\delta$  C–H<sub>CH<sub>3</sub>group</sub>) and stronger bands at 1598  $\text{cm}^{-1}$  ( $\delta$  O–H +  $\nu$  C–H<sub>ar</sub> +  $\nu$  C=C<sub>ar</sub>) and 1304  $\text{cm}^{-1}$  ( $\nu$  SO<sub>2</sub>).

## Solubility study

The solubility profile of meloxicam and cocrystals is shown in Fig. 11. All crystalline material showed a maximum concentration of the drug at 18 h, followed by a

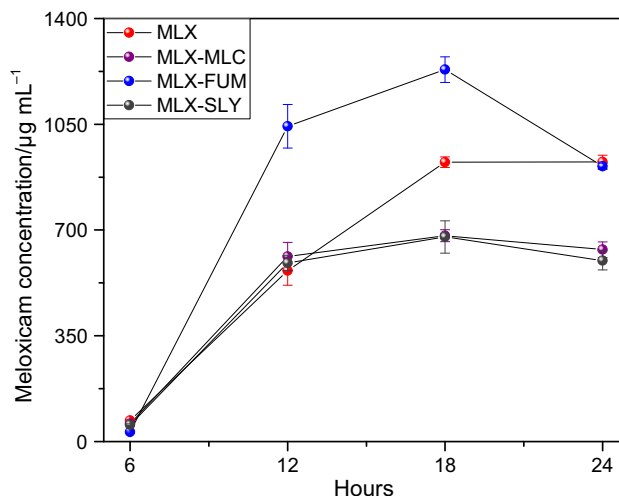


Fig. 11 Solubility test of meloxicam and cocrystals (pH 6.5 and 37 °C)

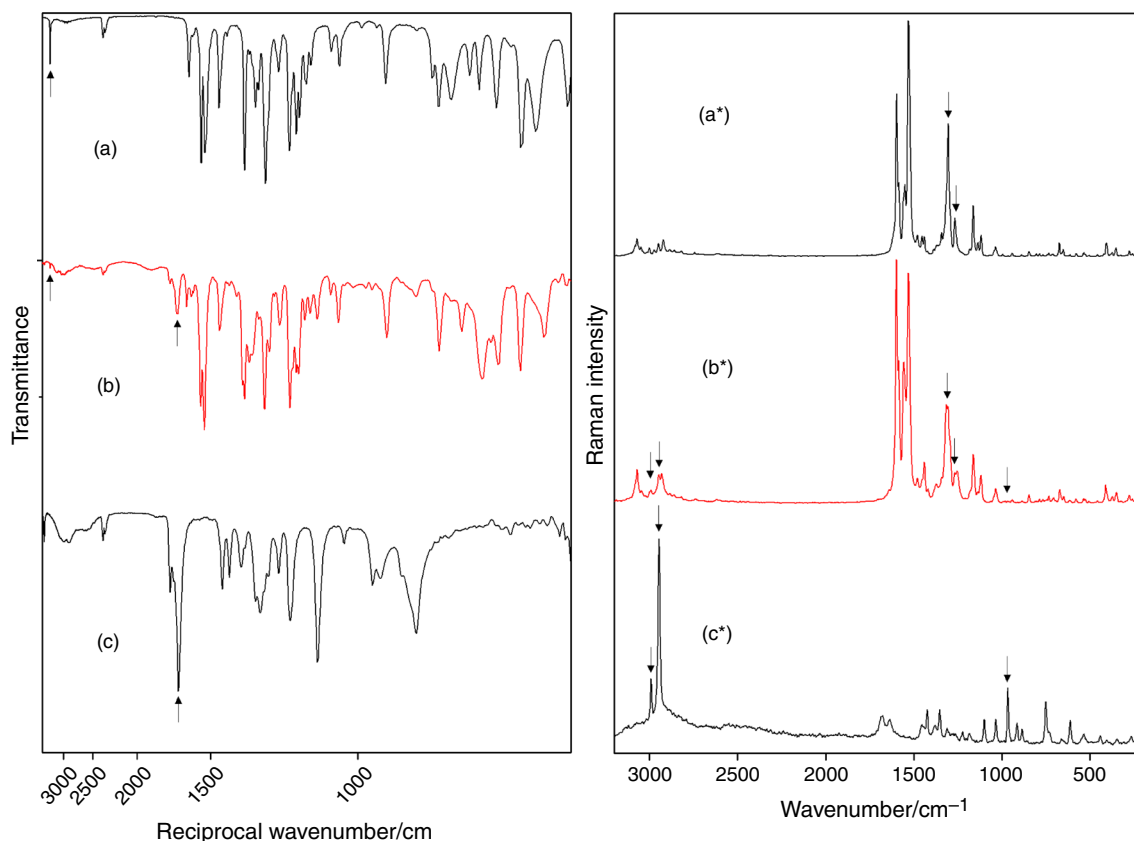


Fig. 10 FTIR and Raman\* spectra for (a, a\*) MLX, (b, b\*) MLX/MLC (1:1) cocrystal, and (c, c\*) MLC

decrease in meloxicam concentration, described as “spring and parachute” [29]. The mechanism is explained by the presence of the coformer, which presents higher solubility than the drug and is drawn out of the crystal lattice. The API (hydrophobic molecule) becomes supersaturated in aqueous medium and has higher energy compared to crystalline phase, showing higher solubility than the pure drug. This high-energy phase becomes the stable form over time (crystalline API), losing solubility.

MLX/FUM system shows higher solubility in most part of the experiment, with 84% and 33% higher meloxicam concentration at 12 and 18 h when compared to the API. MLX/MLC and MLX/SLY show similar result with the pure drug before 12 h and minor meloxicam concentration after 18 h when compared to MLX.

## Conclusions

The study of the compounds by the thermo-analytical techniques established the fingerprint of the cocrystals formed. Also, observation of the thermal behavior of each of the components individually and together made it possible to visualize the changes in the thermal stabilities due to the hydrogen interactions formed in the cocrystals.

The DSC-photovisual analysis helped to understand the phenomena that occur during the heating of the systems and to verify changes in the characteristics of the cocrystals. The cyclic DSC enabled observation of an irreversible polymorphic transition in the MLX/MLC (1:1) cocrystal with subsequent confirmation by XRD before and after the transition.

Observation and more detailed study of the compound malic acid allowed the discovery of two degradation products, confirmed by FTIR, in the collected materials and the proposition of a reaction mechanism that explained the formation of fumaric and maleic acids.

The powder X-ray patterns confirmed the formation of cocrystals, and spectroscopic techniques helped identify which localities allowed the interaction between coformers and API. FTIR and Raman spectroscopy suggest a group interaction due to the decrease in some absorption bands and show hydrogen bonds between NH, OH, and CO groups in the cocrystals.

Mechanochemistry methods together with the use of the ethanol solvent were effective, considering the ease and low cost of the method when compared to methodologies that use a high volume of solvent or high temperature to form cocrystals.

Solubility test of the materials has shown that FUM/MLX cocrystal exhibited a greater meloxicam concentration compared to API, showing that cocrystallization can

provide solutions to overcome poorly soluble drug problems in the pharmaceutical field.

**Acknowledgements** The authors thank CPID/CDMF, FAPESP (Proc. Nos. 2017/14936-9, 2018/12463-9 and 2018/24378-6), CNPq (Proc. 141829/2017-6), and CAPES foundations (Brazil) for financial support.

## References

1. Healy AM, Worku ZA, Kumar D, Madi AM. Pharmaceutical solvates, hydrates and amorphous forms: a special emphasis on cocrystals. *Adv Drug Deliv Rev.* 2017;117:25–46. <https://doi.org/10.1016/j.addr.2017.03.002>.
2. Cerreia Vioglio P, Chierotti MR, Gobetto R. Pharmaceutical aspects of salt and cocrystal forms of APIs and characterization challenges. *Adv Drug Deliv Rev.* 2017;117:86–110. <https://doi.org/10.1016/j.addr.2017.07.001>.
3. Berry DJ, Steed JW. Pharmaceutical cocrystals, salts and multi-component systems; intermolecular interactions and property based design. *Adv Drug Deliv Rev.* 2017;117:3–24. <https://doi.org/10.1016/j.addr.2017.03.003>.
4. FDA. Guidance for industry regulatory classification of pharmaceutical co-crystals guidance for industry regulatory classification of pharmaceutical co-crystals. Rockville: Federal Register FDA; 2013. p. 1–5.
5. Lara-Ochoa F, Espinosa-Pérez G. Cocrystals definitions. *Supramol Chem.* 2007;19:553–7. <https://doi.org/10.1080/10610270701501652>.
6. Aakeröy CB, Chopade PD. Cocrystals: synthesis, structure, and applications. In: Gale PA, Steed JW, editors. *Supramolecular chemistry: from molecules to nanomaterials*. Wiley, Chichester, 2012. <https://doi.org/10.1002/9780470661345.smc113>.
7. Thayer AM. Finding solutions. *Chem Eng News.* 2010;88:13–8. <https://doi.org/10.1037/e537622009-002>.
8. Babu NJ, Nangia A. Solubility advantage of amorphous drugs and pharmaceutical cocrystals. *Cryst Growth Des.* 2011;11:2662–79. <https://doi.org/10.1021/cg200492w>.
9. Cheney ML, Weyna DR, Shan N, Hanna M, Wojtas L, Zaworotko MJ. Supramolecular architectures of meloxicam carboxylic acid cocrystals, a crystal engineering case study. *Cryst Growth Des.* 2010;10:4401–13. <https://doi.org/10.1021/cg100514g>.
10. Myz SA, Shakhtshneider TP, Fucke K, Fedotov AP, Boldyreva EV, Boldyrev VV, Kuleshova NI. Synthesis of co-crystals of meloxicam with carboxylic acids by grinding. *Mendeleev Commun.* 2009;19:272–4. <https://doi.org/10.1016/j.mencom.2009.09.014>.
11. Weyna DR, Cheney ML, Shan N, Hanna M, Zaworotko MJ, Sava V, Song S, Sanchez-Ramos JR. Improving solubility and pharmacokinetics of meloxicam via multiple-component crystal formation. *Mol Pharm.* 2012;9:2094–102. <https://doi.org/10.1021/mp300169c>.
12. Kaufman TS, Vignaduzzo S, Castellano P. Development and validation of a dissolution test for meloxicam and pridinol mesylate from combined tablet formulation. *Indian J Pharm Sci.* 2010;72:197. <https://doi.org/10.4103/0250-474x.65033>.
13. Takagi T, Ramachandran C, Bermejo M, Yamashita S, Yu LX, Amidon GL. A provisional biopharmaceutical classification of the top 200 oral drug products in the United States, Great Britain, Spain, and Japan. *Mol Pharm.* 2006;3:631–43. <https://doi.org/10.1021/mp0600182>.

14. Han H-K, Choi H-K. Improved absorption of meloxicam via salt formation with ethanolamines. *Eur J Pharm Biopharm.* 2007;65:99–103. <https://doi.org/10.1016/j.ejpb.2006.07.003>.
15. Defazio S, Cini R. Synthesis, x-ray structure and molecular modelling analysis of cobalt(ii), nickel(ii), zinc(ii) and cadmium(ii) complexes of the widely used anti-inflammatory drug meloxicam. *J Chem Soc Dalton Trans.* 2002. <https://doi.org/10.1039/b107594m>.
16. Ghorab MM, Abdel-Salam HM, El-Sayad MA, Mekhel MM. Tablet formulation containing meloxicam and  $\beta$ -cyclodextrin: mechanical characterization and bioavailability evaluation. *AAPS PharmSciTech.* 2004;5:63–8. <https://doi.org/10.1208/pt050459>.
17. Luger P, Daneck K, Engel W, Trummelitz G, Wagner K. Structure and physicochemical properties of meloxicam, a new NSAID. *Eur J Pharm Sci.* 1996;4:175–87. [https://doi.org/10.1016/0928-0987\(95\)00046-1](https://doi.org/10.1016/0928-0987(95)00046-1).
18. Variankaval N, Wenslow R, Murry J, Hartman R, Helmy R, Kwong E, Clas S-D, Dalton C, Santos I. Preparation and solid-state characterization of nonstoichiometric cocrystals of a phosphodiesterase-IV inhibitor and  $\alpha$ -tartaric acid. *Cryst Growth Des.* 2006;6:690–700. <https://doi.org/10.1021/cg050462u>.
19. Chen AM, Ellison ME, Peresyppin A, Wenslow RM, Variankaval N, Savarin CG, Natishan TK, Mathre DJ, Dormer PG, Euler DH, Ball RG, Ye Z, Wang Y, Santos I. Development of a pharmaceutical cocrystal of a monophosphate salt with phosphoric acid. *Chem Commun.* 2007;4:419–21. <https://doi.org/10.1039/b612353h>.
20. Schultheiss N, Newman A. Pharmaceutical cocrystals and their physicochemical properties. *Cryst Growth Des.* 2009;9:2950–67. <https://doi.org/10.1021/cg900129f>.
21. Frišćić T, Childs SL, Rizvi SAA, Jones W. The role of solvent in mechanochemical and sonochemical cocrystal formation: a solubility-based approach for predicting cocrystallisation outcome. *CrystEngComm.* 2009;11:418–26. <https://doi.org/10.1039/B815174A>.
22. United States Pharmacopeia, USP 36—Chapter 1092—The Dissolution Procedure, (2013) 1–28.
23. Franzé JA, Carvalho TF, Gaglieri C, Caires FJ, Bannach G, Castro RC, Treu-Filho O, Ionashiro M, Mendes RA. Synthesis, characterization, thermal and spectroscopic studies and bioactivity of complexes of meloxicam with some bivalent transition metals. *J Therm Anal Calorim.* 2017;127:1393–405. <https://doi.org/10.1007/s10973-016-6030-5>.
24. Karagianni A, Malamatarí M, Kachrimanis K. Pharmaceutical cocrystals: new solid phase modification approaches for the formulation of APIs. *Pharmaceutics.* 2018;10:1–30. <https://doi.org/10.3390/pharmaceutics10010018>.
25. Cherukuvada S, Guru Row TN. Comprehending the formation of eutectics and cocrystals in terms of design and their structural interrelationships. *Cryst Growth Des.* 2014;14:4187–98. <https://doi.org/10.1021/cg500790q>.
26. Ionashiro EY, Caires FJ, Siqueira AB, Lima LS, Carvalho CT. Thermal behaviour of fumaric acid, sodium fumarate and its compounds with light trivalent lanthanides in air atmosphere. *J Therm Anal Calorim.* 2012;108:1183–8. <https://doi.org/10.1007/s10973-011-1660-0>.
27. Kim S, Thiessen PA, Bolton EE, Chen J, Fu G, Gindulyte A, Han L, He J, He S, Shoemaker BA, Wang J, Yu B, Zhang J, Bryant SH. PubChem substance and compound databases. *Nucl Acids Res.* 2016;44:D1202–13. <https://doi.org/10.1093/nar/gkv951>.
28. Giron D. Monitoring of polymorphism—from detection to quantification. *Eng Life Sci.* 2003;3:103–12. <https://doi.org/10.1002/elsc.200390012>.
29. Bavishi DD, Borkhataria CH. Spring and parachute: how cocrystals enhance solubility. *Prog Cryst Growth Charact Mater.* 2016;62:1–8. <https://doi.org/10.1016/j.pcrysgrow.2016.07.001>.

**Publisher's Note** Springer Nature remains neutral with regard to jurisdictional claims in published maps and institutional affiliations.